Toward 2D dynamo models calibrated by global 3D relativistic accretion disk simulations

Matthew D. Duez,[1] Courtney L. Cadenhead,[1] Zachariah B. Etienne,[2] Bernard Kelly,[3,4,5] and Leonardo R. Werneck[2]

[1]*Department of Physics and Astronomy, Washington State University, Pullman, Washington 99164, USA*
[2]*Department of Physics, University of Idaho, Moscow, Idaho 83844, USA*
[3]*Center for Space Sciences and Technology, University of Maryland, Baltimore County, 1000 Hilltop Circle Baltimore, Maryland 21250, USA*
[4]*Gravitational Astrophysics Laboratory, NASA Goddard Space Flight Center, Greenbelt, Maryland 20771, USA*
[5]*Center for Research and Exploration in Space Science and Technology, NASA Goddard Space Flight Center, Greenbelt, Maryland 20771, USA*

(Received 5 September 2024; accepted 2 January 2025; published 22 January 2025)

Two-dimensional models assuming axisymmetry are an economical way to explore the long-term evolution of black hole accretion disks, but they are only realistic if the feedback of the nonaxisymmetric turbulence on the mean momentum and magnetic fields is incorporated. Dynamo terms added to the 2D induction equation should be calibrated to 3D magnetohydrodynamics simulations. For generality, the dynamo tensors should be calibrated as functions of local variables rather than explicit functions of spatial coordinates in a particular basis. In this paper, we study the feedback of nonaxisymmetric features on the 2D mean fields using a global 3D, relativistic, Cartesian simulation from the IllinoisGRMHD code. We introduce new methods for estimating overall dynamo α and turbulent diffusivity effects, as well as measures of the dominance of nonaxisymmetric components of energies and fluxes within the disk interior. We attempt closure models of the dynamo electromotive force using least-squares fitting, considering both models where coefficient tensors are functions of space and more global, covariant models. None of these models are judged satisfactory, but we are able to draw conclusions on what sorts of generalizations are and are not promising.

DOI: 10.1103/PhysRevD.111.023040

I. INTRODUCTION

A. The accretion disk dynamo problem

Untilted black hole accretion disks are three-dimensional, turbulent systems, but their fluid and field profiles can be viewed as combinations of an axisymmetric, slowly evolving "background" and nonaxisymmetric "fluctuations." Often, only the background is of interest, with fluctuations considered primarily for their feedback effects on the background. This perspective motivates the use of 2D (axisymmetric) simulations to model accretion flows.

Simply evolving the general relativistic magnetohydrodynamic (GRMHD) equations in 2D will almost certainly be inadequate; magnetohydrodynamic (MHD) flows are often not only quantitatively but even qualitatively different in 2D vs 3D, as illustrated by opposite turbulent energy cascades [1,2] and the 2D antidynamo theorem [3,4]. What is desired are 2D evolutions that "look like" 3D evolutions. Even this goal is ambiguous. It might mean 2D evolutions that resemble the azimuthal average of 3D evolutions, or it might mean 2D evolutions that resemble representative 2D slices of 3D evolutions. Both approaches might be interesting, but they will likely be very different. Given these differences, one must choose when designing a model whether the 2D fields represent azimuthal averages or a representative slice. For this paper, we consider 2D models of azimuthally averaged 3D evolutions.

Filtering away the fluctuating component alters the evolution equations, as can be seen by azimuthally averaging the Newtonian induction equation

$$\begin{aligned}\overline{\partial_t \boldsymbol{B}} &= \overline{\boldsymbol{\nabla} \times (\boldsymbol{B} \times \boldsymbol{v})} \\ &= \boldsymbol{\nabla} \times (\overline{\boldsymbol{B} \times \boldsymbol{v}}) \\ &\equiv \boldsymbol{\nabla} \times (\bar{\boldsymbol{B}} \times \bar{\boldsymbol{v}} + \boldsymbol{\Delta E}).\end{aligned} \tag{1}$$

To evolve these equations, a closure condition is needed, providing the dynamo electromotive force (EMF) $\boldsymbol{\Delta E}$ as a function of azimuthally averaged variables. A commonly considered closure [4,5] is

$$\Delta E^i = \alpha^i_j B^j + \eta^i_j J^j \tag{2}$$

where J^j is the current, B^j is the magnetic field, α^i_j is the dynamo α tensor, and η^i_j is the turbulent magnetic diffusivity tensor.

B. Past work

Dynamo corrections to 2D GRMHD simulations have been undertaken by a number of groups [6–10], usually assuming an isotropic dynamo, for which $\alpha^i_j = \alpha_{\rm dyn}\delta^i_j$ and $\eta^i_j = \eta_{\rm dyn}\delta^i_j$. The $\alpha_{\rm dyn}$ term enables the dynamo α effect, i.e., a toroidal field produces a poloidal field. The α effect enables 2D GRMHD simulations to maintain magnetic fields at the strength seen in 3D simulations. (Note that using it for this reason implies a representative 2D slice rather than an azimuthal average interpretation.) The $\eta_{\rm dyn}$ term is the turbulent magnetic diffusivity, which acts like a resistivity. As $\alpha_{\rm dyn}$ is a pseudoscalar, it is expected to switch sign at the equator, so some such spatial dependence on $\alpha_{\rm dyn}$ is often stipulated.

Dynamo terms are also sometimes added to 3D GRMHD simulations [11–14]. In this case, the distinction between background and fluctuation (and hence the meaning of averaging) is done differently—the fluctuation is the MHD flow at spatial scales below the grid scale. It is not clear *a priori* if the same $\boldsymbol{\Delta E}$ model should apply to the two cases.

Three-dimensional MHD simulations can be used to extract α^i_j and η^i_j. Brandenburg and Donner [15] estimate $\alpha_{\rm dyn}$, defined as $\alpha_{\rm dyn} \equiv \Delta E_\phi / B_\phi$, from shearing box simulations. Gressel and Pessah [16] calculated the full α^i_j and η^i_j tensors using a test-field method. They studied shearing box simulations and averaged over boxes, so their distinction between mean and fluctuating fields was not quite the same as the azimuthal average, but they were able to study dependence on shear and vertical field. Hogg and Reynolds [17] used global MHD simulations to extract $\alpha_{\rm dyn}$ in each hemisphere. Bendre *et al.* [18] introduced a method of extracting α^i_j and η^i_j by least-squares fitting via singular value decomposition (SVD), which they applied to radiatively inefficient accretion disks in Dhang *et al.* [19]. Both test-field and SVD methods find deviations in dynamo tensors from isotropy and report fairly consistent magnitudes. Dhang *et al.* note the difficulty of extracting a clear dynamo signal in the disk region, as well as other indications that the field and flow are mostly nonaxisymmetric. The SVD method has also been used for solar dynamo and binary neutron star remnant calculations [20,21].

The recent study by Jacquemin-Ide *et al.* [22], using GRMHD disk simulations to study dynamo action from the nonlinear evolution of the magnetorotational instability, also presents some relevant findings. They reported that $m = 1$ to $m = 3$ modes (decomposing azimuthal dependence into $e^{im\phi}$ Fourier modes) are crucial in dynamo generation of poloidal field. They also emphasize the importance of magnetic flux advection from the outer to the inner disk. This might be a less prominent effect in the small disks (resembling short γ-ray burst setups) often studied in compact binary merger contexts. Finally, they do estimate the viability of an $\alpha_{\rm dyn}$ and $\eta_{\rm dyn}$ dynamo closure using correlation coefficients between ΔE_ϕ and B_ϕ or J_r. The average $\Delta E_\phi - B_\phi$ correlation oscillates about zero and does not show a significant time average; the $\Delta E_\phi - J_r$ correlation does have a time average clearly distinct from zero, but is strongest with a time offset between cause and effect, suggesting it is mediated by additional dynamics.

C. Remaining issues

The number of studies that extract dynamo coefficients from global disk simulations, particularly relativistic simulations, remains small given the parameter space of disk states, and not all existing results have high statistical significance. Furthermore, dynamo coefficient extraction is of two types: either a single average coefficient is extracted for the entire disk (or a hemisphere thereof), or dynamo coefficients are extracted at each (r, θ) point in space. These spatial dependencies are presumably proxies for dependence on the local physical quantities and their derivatives. If these dependencies could be made explicit, the resulting model for ΔE^i with only a few global fitting constants (as opposed to fitting scalar functions of space) could be expressed in covariant tensor form, making it immediately generalizable to general spatial coordinate systems and more easily generalizable to other accretion systems (varying disk thickness, magnetic flux, and rotation law).

Another concern with existing closure models is that the distinction between background and fluctuating turbulence is too sharp. In terms of the Fourier decomposition of fields in the azimuthal direction, it seems safer to distinguish high-m modes from the background than, for example, $m = 1$ or $m = 2$ modes. A possible criterion would be to consider an $m \neq 0$ mode is "turbulent" only if the eddy turnover time is less than the orbital period. For simplicity, consider unmagnetized incompressible turbulence with turbulent velocity $\sim v_T$ at the largest length scale H (the disk scale height) and the usual Kolmogorov energy cascade. At scale ℓ, the velocity scale is v_ℓ and the timescale is $\tau_\ell \approx \ell / v_\ell$. As specific kinetic energy density flows to lower scales at the same rate $\approx v_\ell^2/\tau_\ell$ for all ℓ, it follows that $\tau_\ell \approx H^{1/3}\ell^{2/3}v_T^{-1}$. Turbulent modes then have $\tau_\ell < \Omega^{-1}$, where Ω is the orbital frequency. Estimating $m \approx R/\ell$ at radius R, the eddy time is then sufficiently short if

$$m > m_{\rm crit} \approx RH^{1/2}(\Omega/v_T)^{3/2}. \tag{3}$$

It might be necessary to evolve $m < m_{\rm crit}$ (which could be considered a compromise between 2D and 3D, assuming $m_{\rm crit}$ turns out to be a small number), with the $m > m_{\rm crit}$ contribution safely modeled by a turbulent/dynamo closure. From the results of Jacquemin-Ide *et al.* [22] mentioned above, we might guess $m_{\rm crit} \approx 3$.

D. This paper

In this paper, we present a new analysis of the azimuthally averaged evolution of a magnetorotationally turbulent disk around a Kerr black hole. We use data from the Cartesian numerical relativity code IllinoisGRMHD [23,24]. We present a detailed analysis of the degree of nonaxisymmetry, introducing measures of its dominance in magnetic energy, kinetic energy, and angular momentum transport. We find that most of the magnetic field and nonazimuthal velocity field are averaged out by azimuthal averaging, and momentum transport is predominantly nonaxisymmetric. Thus, azimuthally averaged 3D ideal GRMHD resembles viscous hydrodynamics more than 2D ideal GRMHD. We also propose ways of estimating an average $\alpha_{\rm dyn}$ and $\eta_{\rm dyn}$. An elegant definition of the former comes from the Lorentz invariants of the azimuthally averaged field tensor. For the latter, we take advantage of the fact that, at least for the first $\sim 10,000M$, 2D ideal GRMHD overpredicts the magnetic energy compared to azimuthally averaged 3D GRMHD, so we estimate $\eta_{\rm dyn}$ by the resistivity needed to achieve this level of field suppression. For this purpose, we add a new phenomenological resistivity to the HARM [24,25] code and compare with the 3D results.

Next, we attempt to extract α^i_j and η^i_j using SVD least-squares fitting. We consider models for which coefficients are functions of (r,θ), functions of θ, or functions of local scalars and pseudoscalars (with spacetime dependency only from those scalars and pseudoscalars). We introduce norms for the error in the best-fit model and variance in coefficient extraction to easily assess the reliability of models. None of the models meet all of our preset standards.

Since these models assuming Eq. (2) are not judged satisfactory, we assess certain alternative classes of models which maintain the same basic structure of the dynamo EMF. First, we consider whether a successful global model could be created if the root-mean-squared (rms) deviation from axisymmetry of the velocity or magnetic field were known. To be usable as a closure condition, an evolution equation for one of these variables that tracks the true evolution well enough would have to be introduced, similar to the evolution of the mean turbulent kinetic energy in $k-\epsilon$ models [2,26,27] (which might be generalized to MHD [28,29]). In fact, such scalars do not provide acceptable dynamo models, so the motivation to devise such evolution equations does not arise. Second, we ask whether the residual EMF, subtracting off the EMF computed from $m=0$ to $m=3$ components of $\boldsymbol{v}$ and $\boldsymbol{B}$, is more amenable to dynamo models of the form Eq. (2). It is not. We conclude that more general models for ΔE^i are likely required.

This paper is organized as follows. In Sec. II, we review the GRMHD and dynamo equations. In Sec. III, we provide details on the 3D simulation, in particular, analyzing the contributions of nonaxisymmetric fields. In Sec. IV, we describe how to produce estimates of the isotropic $\alpha_{\rm dyn}$, $\eta_{\rm dyn}$. In Sec. V, we describe how we produce fits to α^i_j, η^i_j and present quality of fits. We summarize our results in Sec. VI and present conclusions in Sec. VII.

We use geometrized units ($G=c=1$) throughout. Latin letters from the beginning of the alphabet (a–f) are spacetime indices, running 0–3. Indices i, j, k are spatial, running 1–3. When writing equations in geometric form, vectors and forms are written in boldface, with 2-forms getting a "2" superscript prefix (e.g., ${}^2\boldsymbol{B}$).

II. AN ANALYTIC DYNAMO MODEL

In this section, we derive a relativistic version of the Newtonian dynamo closure equation (2) which will be used in subsequent sections. For use in a relativistic code, the dynamo closure condition must at least be spatially covariant; this will account for the unpredictable evolution of the coordinate system or the deliberate use of curvilinear coordinates or coordinates with designed radial or angular concentrations. Azimuthal averaging introduces a preferred direction, the azimuthal Killing vector $\boldsymbol{e_\phi} \equiv \partial/\partial\phi$, which generally will leave an imprint in the $\boldsymbol{\alpha}$ and $\boldsymbol{\eta}$ tensors, so that 3D covariant equations for these tensors will be expected to include $\boldsymbol{e_\phi}$. Whether the equation must be 4D covariant, i.e., Lorentz covariant, is more debatable. It could be argued that the averaging procedure itself, which is defined to be azimuthal average at a fixed time, breaks Lorentz invariance. Indeed, subgrid and effective viscosity prescriptions that are purely spatial, which have been widely and successfully used in numerical relativity [30], can have similar justifications. On the other hand, in one case, we found it important to keep terms first order in velocity to properly recover the Newtonian limit [31].

Assume a foliation of the spacetime with the usual normal to the slice $\tilde{\boldsymbol{n}} = -N\tilde{\boldsymbol{dt}}$ and 3-metric $\gamma_{ab} = g_{ab} + n_a n_b$, where N is the lapse function. The field tensor associated with the azimuthally averaged fields is

$$F^{ab} = n^a \bar{E}^b - n^b \bar{E}^a + \epsilon^{abc}\bar{B}_c, \tag{4}$$

$$\star F^{ab} = \bar{B}^a n^b - \bar{B}^b n^a + \epsilon^{abc}\bar{E}_c, \tag{5}$$

where $\bar{E}\cdot n = \bar{B}\cdot n = 0$, and $\epsilon^{abc} = n_d \epsilon^{abcd}$. (Here $\epsilon^{abcd} = |g|^{-1/2}[abcd]$ is the Levi-Civita tensor and $[abcd]$ is the totally antisymmetric Levi-Civita symbol.)

The fluid frame is defined by the azimuthally averaged 4-velocity u^a, which can be decomposed as $u^a \equiv W n^a + \mathcal{V}^a$, where W is the Lorentz factor and $\boldsymbol{\mathcal{V}}$, defined so $\mathcal{V}^a n_a = 0$, is the Eulerian velocity, not the transport velocity. For the rest of this section, we will suppress lines above averaged quantities, assuming that all quantities are azimuthal averages.

The electric field ${}^u E^a$ in the fluid frame, which is also the Lorentz force, is

$$ {}^{u}E^{a} \equiv F^{ab}u_b = WE^a + n^a E^b \mathcal{V}_b + \epsilon^{abc}\mathcal{V}_b B_c. \quad (6) $$

In ideal MHD, this is zero, and the components parallel and perpendicular to $\boldsymbol{n}$ must independently vanish, so

$$ {}^{\mathrm{MHD}}E^a = -\frac{1}{W}\epsilon^{abc}\mathcal{V}_b B_c. \quad (7) $$

One can also compute the electric field using the transport velocity 3-vector $v^i \equiv u^i/u^t$ (cf. [32]),

$$ E_i = -\frac{1}{N}\epsilon_{ijk}(v^j + \beta^j)B^k, \quad (8) $$

where β^i is the shift vector.

In the fluid frame, the magnetic field is

$$ {}^{u}B^a = -\star F^{ab}u_b = WB^a + B^b\mathcal{V}_b n^a - \epsilon^{abc}\mathcal{V}_b E_c. \quad (9) $$

A covariant expression that recovers the Newtonian limit [Eq. (2)] is

$$ F^{ab}u_b = -\alpha^{au}_b B^b + \eta^a_b \epsilon^{cbde}u_c \nabla_d {}^{u}B_e. \quad (10) $$

Note that, in the last term, we can switch freely between ∇ and ∂ since d and e are antisymmetrized.

Another possibility would have been to use the actual current

$$ F^{ab}u_b = -\alpha^{au}_b B^b + \eta^{au}_b J^b, \quad (11) $$

which is different from the previous equation because of the displacement current $\mathcal{L}_{\boldsymbol{n}}\boldsymbol{E}$ term in Ampère's law. However, the identification of the diffusivity term with $\boldsymbol{\nabla}\times\boldsymbol{B}$ should be considered more fundamental than its identity with $\boldsymbol{J}$, because it is motivated by an expansion in terms of one over the length scale of the magnetic field. Hereafter, we will simply denote the curl of $\boldsymbol{B}$ as $\boldsymbol{J}$.

Unfortunately, Eq. (9) itself has the electric field in it. Luckily, this term is proportional to velocity and subdominant in most regions. For a dynamo equation with only an isotropic $\boldsymbol{\alpha}$ tensor ($\eta^a_b = 0$), Most has shown that one can solve for E^a analytically without needing to assume small velocity [14]. Instead, we will substitute the ideal MHD electric field [Eq. (7)] in the $\boldsymbol{\eta}$ term, so that the weak dynamo case is properly recovered. Then

$$ \begin{aligned} {}^{u}B^a &= WB^a + B^b\mathcal{V}_b n^a - \epsilon^{abc}\mathcal{V}_b(-W^{-1})\epsilon_{cef}\mathcal{V}^e B^f \\ &= B^b\mathcal{V}_b n^a + \frac{1}{W}[B^a + B^b\mathcal{V}_b\mathcal{V}^a], \end{aligned} \quad (12) $$

where we have used $W^2 = 1 + \mathcal{V}^2$. As for the curl term in Eq. (10), we find

$$ \epsilon^{abcd}u_a\partial_c {}^{u}B_d = -W\epsilon^{bcd}\partial_c {}^{u}B_d + \epsilon^{abcd}\mathcal{V}_a\partial_c {}^{u}B_d. \quad (13) $$

The first is just a spatial curl, albeit of the boosted B, which is easy to compute. The second term is, in general, difficult to calculate because it will include time derivatives which are less easily available to an evolution code or postprocessing analysis. However, in most cases, this term will be small. Consider cases in which $\mathcal{V}^i$ and n^i are small enough (implying that the shift vector is small, which is usually the case when not very close to a black hole for commonly chosen gauge conditions) that one can keep only terms at lowest order in these without great loss of accuracy. Then $\mathcal{V}_0 = B_0 = 0$, and for spatial components of the free index b the index c must be the one that is the time component. In the weak dynamo limit, the time derivative of B^a is proportional to $\mathcal{V}^i$, and for slowly evolving metrics, $\partial_t B_a$ is proportional to $\partial_t B^b$. So this term, which looks first order in $\mathcal{V}$, is actually second order, and will be dropped. We also drop the term $B^b\mathcal{V}_b n^a$ in ${}^{u}B^a$ [see Eq. (12)] as second order.

For the component of Eq. (10) perpendicular to $\boldsymbol{n}$, and using (6), we are left with our final result,

$$ \begin{aligned} WE^a = &-\epsilon^{abc}\mathcal{V}_b B_c - \alpha^a_b W^{-1}[B^b + B^c\mathcal{V}_c\mathcal{V}^b] \\ &- \eta^a_b W\epsilon^{bed}\partial_e[(B_d + B^c\mathcal{V}_c\mathcal{V}_d)W^{-1}]. \end{aligned} \quad (14) $$

Equation (14) is a relativistic generalization of Eq. (2). It provides the dynamo model to which we will attempt to fit our azimuthally averaged 3D simulation data. The first term on the right-hand side is the ideal MHD term. The remaining terms are $W\Delta E^a$.

III. NONAXISYMMETRIC FEATURES OF THE 3D SIMULATION

A. Methods of 3D simulation

The simulation we used was produced as part of the Event Horizon GRMHD code comparison project [33]. The fixed spacetime is a Kerr black hole with dimensionless spin parameter $a/M = 0.9375$. The gas is an ideal gas with adiabatic index $\Gamma = 4/3$. The initial state of the gas has constant specific angular momentum, defined as $\ell = u^t u_\phi$. In the absence of magnetic forces, the gas forms an equilibrium torus with an inner radius of $6M$ and maximum density at $12M$. We seed a magnetic field at $t = 0$, with the maximum of the magnetic pressure $P_B^{\max}$ and the maximum of the gas pressure $P_{\mathrm{gas}}^{\max}$ related as $P_B^{\max}/P_{\mathrm{gas}}^{\max} = 100$. The field is calculated from a toroidal vector potential $A_\phi \propto \max(\rho/\rho_{\max} - 0.2, 0)$. This initial state produces a "standard and normal evolution" (SANE) accretion flow, i.e., one for which magnetic flux on the horizon does not significantly affect accretion.

The IllinoisGRMHD [23,24] simulation uses a Cartesian fixed mesh refinement (FMR) grid (utilizing the cactus/carpet infrastructure), in which the coarsest grid is a cube with a half side length of $1750M$. There are seven different resolutions used, including six levels of refinement atop this coarse grid, and the finest-grid cube has a resolution

of $\Delta x = \Delta y = \Delta z \approx M/4.388571$. The finest grid is composed of four cubes, each with a half side length of $27.34375M$, and is larger than the black hole, which has a radius of $1.348M$. IllinoisGRMHD evolves a vector potential at cell edges to exactly preserve a finite difference version of the constraint $\nabla \cdot \boldsymbol{B} = 0$ [34]. The magnetized fluid is evolved using a high-resolution shock-capturing scheme, with Piecewise Parabolic Method (PPM) reconstruction and a Harten-Lax-van Leer-Einfeldt (HLLE) approximate Riemann solver.

Table 1 of [33] compares the resolution of the IllinoisGRMHD to others used for the code comparison study. Compared to the low-resolution 96^3 spherical-polar grids, the IllinoisGRMHD run's resolution at maximum density is similar in θ, almost twice as high in r, and about 3 times as high in ϕ. Resolution of the magnetorotational instability (MRI) is quantified by the MRI quality factors, the number of grid points across the wavelength of the fastest growing mode. Taking into account the difference from 96^3 grids reported in Sec. 5.6.3 of [33], we estimate poloidal and toroidal quality factors of $Q^{\rm pol} \sim 4$ and $Q^{\rm tor} \sim 50$, respectively. The poloidal value is less than the ≈ 10 that would be desired for adequate resolution [35]. However, it has been suggested that toroidal resolution can compensate poloidal resolution, and the grid condition should be $Q^{\rm pol}Q^{\rm tor} > 200$ [36,37], which this run barely satisfies. Overall, although turbulence is seen and the MRI is resolved in some regions, it is unresolved in others.

The disk was evolved for a time of $10\,000M$, long enough to see many orbits of fully developed turbulence. Volume data of all evolution variables were stored on a $(N_r, N_\theta, N_\phi) = (150, 75, 64)$ spherical-polar grid. Data were output at a high cadence of $0.57M$, but we find it sufficient to use only every $\Delta t = 100M$ for time averages below. When performing fits for dynamo coefficients, we use time steps separated by $\Delta t = 300M$, where the increased spacing—roughly corresponding to the orbital period at the initial location of maximum density—is chosen to reduce correlation between data at adjacent steps while retaining sufficient data (31 steps), starting at $t = 1000M$, after the magnetic field has become strong and the disk transition from the kinematic to the dynamical regime.

The evolution time is admittedly shorter than usual for dynamo studies. Ordinarily, one would want to observe multiple cycles of the expected dynamo wave. Assuming an $\alpha\Omega$ dynamo with $\alpha_{\rm dyn} \sim 10^{-4}$, a characteristic vertical scale $H \sim 10M$, and a characteristic orbital frequency $\Omega \sim 10^{-2}M^{-1}$, we would expect a dynamo period $\sim\sqrt{H/(\Omega\alpha_{\rm dyn})} \sim 10^4 M$ [5], meaning the full evolution time is not more than a cycle, and we will not be able to produce "butterfly" diagrams of the average toroidal field at different latitudes showing multiple dynamo cycles, as has been done in some longer disk simulations (e.g., [17,38,39]). We will, however, definitely evolve long enough to observe $\boldsymbol{\Delta E}$ acting. Indeed, we will see that during this time, $\boldsymbol{\Delta E}$ exerts a dominant effect on the magnetic field evolution, and the azimuthally averaged field evolves very differently from the corresponding axisymmetric system. We are able to quantify dynamo effects during a part of the cycle but not all parts.

B. Overview of 3D data

We define the following averages:

$$\bar{X}(r,\theta,t) \equiv \frac{1}{2\pi}\int_0^{2\pi} d\phi X(r,\theta,\phi,t), \tag{15}$$

$$\langle X\rangle(r) \equiv \frac{\int_T^{2T} dt \int_{\pi/3}^{2\pi/3} d\theta \int_0^{2\pi} d\phi\sqrt{\gamma}X(r,\theta,\phi,t)}{\int_T^{2T} dt \int_{\pi/3}^{2\pi/3} d\theta \int_0^{2\pi} d\phi\sqrt{\gamma}}, \tag{16}$$

where $T = 5000M$.

To minimize effects of the metric on the spatial dependencies of vector and tensor components, we will use the normed components $X^{\hat{i}} \equiv \sqrt{\gamma_{ii}}X^i$ and $X_{\hat{i}} \equiv \sqrt{\gamma^{ii}}X_i$ when generating plots and fitting formulas. (Note that we drop the Einstein summation convention in the above definitions, so there is no sum over i.)

For a quantity $X(x_A)$, which is a nonlinear function of the primitive variables $x_A = (B^i, v^i, \rho, P)$, define the residual as

$$\Delta X = \bar{X} - X(\bar{x}_A). \tag{17}$$

Suppose instead of retaining only the average of the spherical-polar components of $\boldsymbol{v}$ and $\boldsymbol{B}$, one were to retain the azimuthal Fourier decomposition, truncated at a particular $m = m_t$. Call Ψ_{m_t} the approximation of Ψ with all azimuthal Fourier modes of $m \le m_t$. Then define the residual EMF $\Delta_m \boldsymbol{E} \equiv \overline{\boldsymbol{B}\times\boldsymbol{v}} - \overline{\boldsymbol{B}_m\times\boldsymbol{v}_m}$. Thus, $\boldsymbol{\Delta E} = \Delta_0 \boldsymbol{E}$.

In Fig. 1, we plot azimuthal and time averages of $\Delta E^{\hat{i}}$, $B_{\hat{i}}$, and $J_{\hat{i}}$. A linear relationship between $\Delta E^{\hat{i}}$ and $B_{\hat{i}}$ or $J_{\hat{i}}$ is not immediately suggested to the eye. Of the three vectors, the $B_{\hat{i}}$ components are spatially smoothest, while $J_{\hat{i}}$ show small-scale behavior. $B_{\hat{i}}$ are strongest near the poles, $J_{\hat{i}}$ in the disk, and $\Delta E^{\hat{i}}$ in between.

In Fig. 2, we plot azimuthal and time averages of the components of the transport velocity $v^{\hat{i}}$ and the EMF residual beyond $m = 3$, denoted $\Delta_3 E^{\hat{i}}$ in accord with the notation introduced above. The structure of $\Delta_3 E^{\hat{i}}$ is similar to $\Delta E^{\hat{i}}$, suggesting that the former (representing higher-m modes) significantly contributes to the latter. Velocity is dominated by the disk rotation and the polar outflow; little of the disk turbulence survives the averaging process. We also plot three scalar quantities which might be expected to correlate with $\Delta_3 E^{\hat{i}}$ (but do not), whose discussion we defer to Sec. V C.

C. Nonaxisymmetric energies and fluxes

The azimuthal structure and the effect of azimuthal averaging are illustrated in Fig. 3, in which B^r and E_r

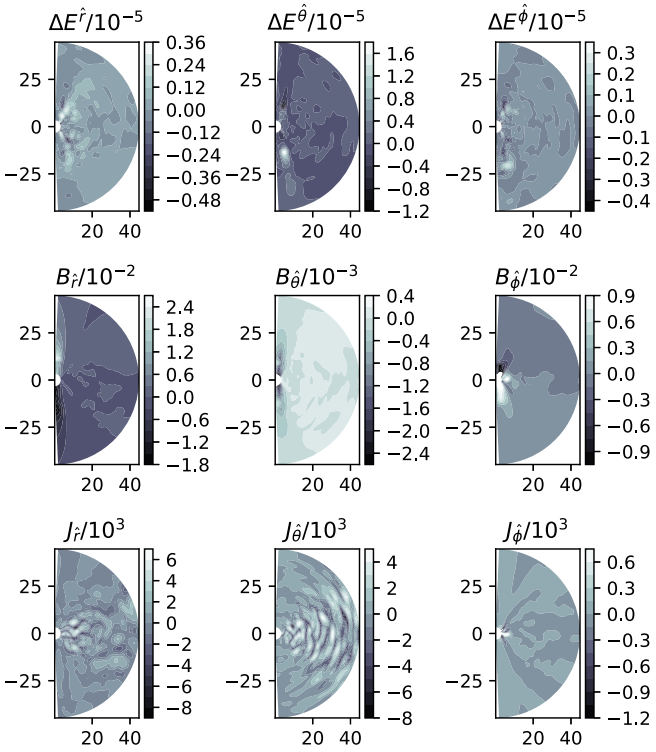

FIG. 1. Azimuthal and time averages of $\Delta E^{\hat{i}}$, $B_{\hat{i}}$, and $J_{\hat{i}}$.

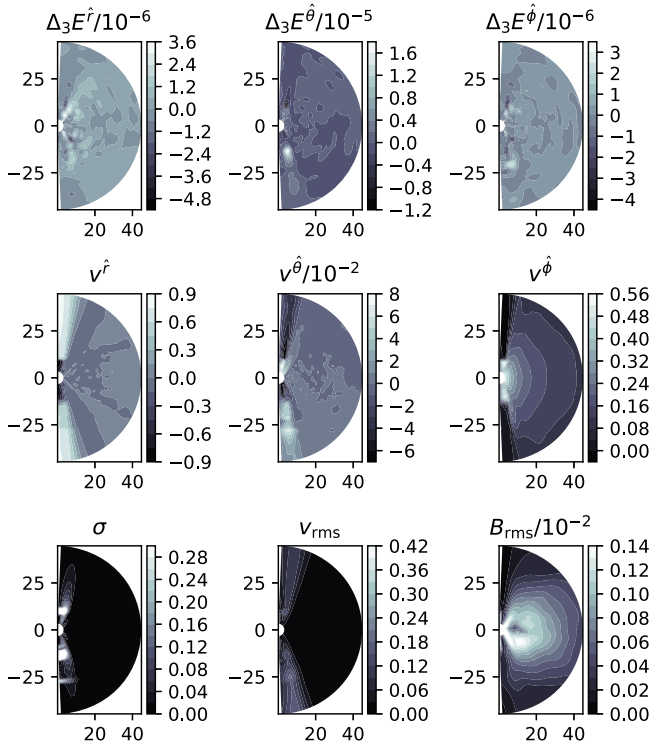

FIG. 2. Azimuthal and time averages of $\Delta_3 E^{\hat{i}}$, $v^{\hat{i}}$, and three scalars: the 2D shear σ and the rms deviations of velocity and magnetic field from their azimuthal mean [see Eq. (48)].

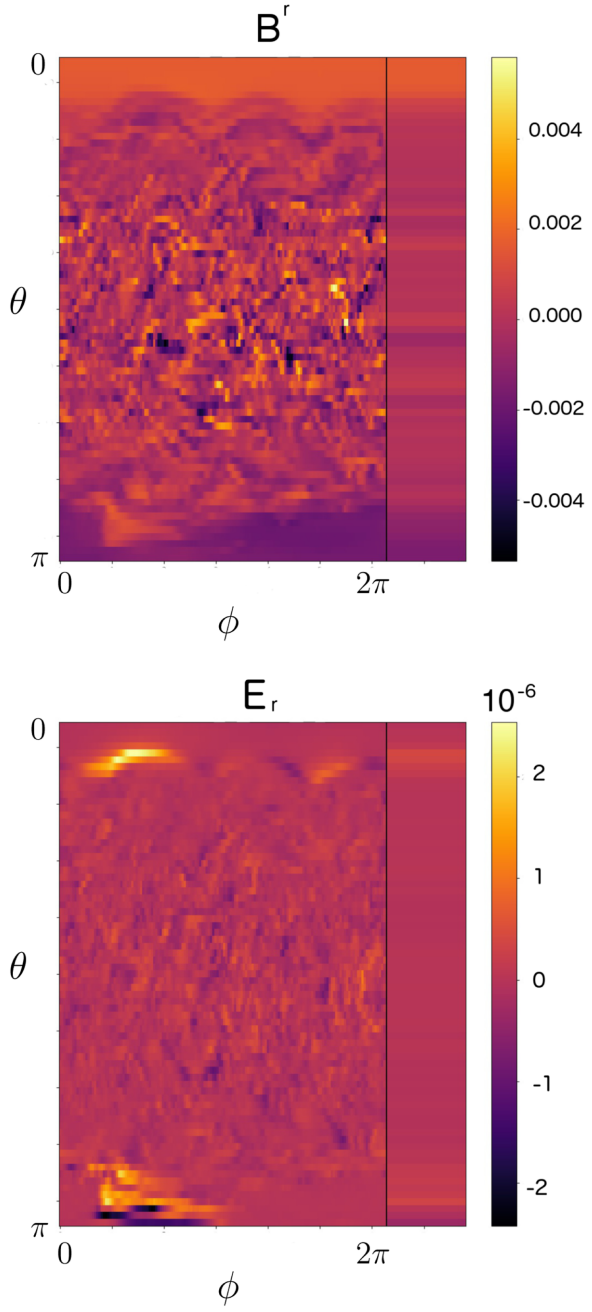

FIG. 3. Latitude-longitude plots of B^r and E_r at radius $r = 25M$ at time $t = 5200M$. As on a standard global map, vertical direction is latitude (with the top corresponding to the North Pole and the bottom to the South Pole), and horizontal direction is longitude. On the right bar, we show the azimuthal average.

are plotted as functions of θ and ϕ at one radius and time. The azimuthal average is shown as a bar on the right. We see that, at least for these quantities, azimuthal mean structure dominates only near the poles. At intermediate latitudes (i.e., in and near the disk), there is small-scale structure (high-m contribution), which averages out to value much smaller than the maximum magnitudes.

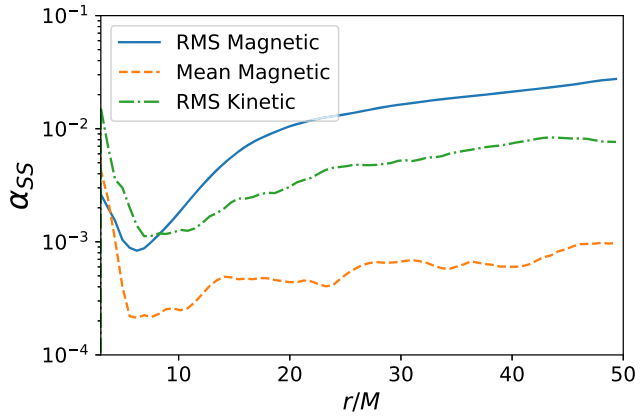

FIG. 4. Time- and angle-averaged momentum fluxes within the disk as functions of r. Magnetic α_{SS} is defined as in Eq. (18) using either the mean magnetic field ("Mean") or the full field with mean subtracted ("rms"), while rms kinetic energy flux uses $t^{r\phi}$ instead of $w^{r\phi}$.

As in [33], we compute the Maxwell stress averaged over time and angle $\langle w^{r\hat{\phi}} \rangle$ as a function of r from the full magnetic field in 3D in two ways: by integrating $b^{\hat{r}} b^{\hat{\phi}}$ in Kerr-Schild coordinates and by integrating in a local frame comoving with the fluid with appropriate comoving volume element. (See [40–42] for details.) We use the frame of the azimuthally averaged velocity for easier comparison with the stress from the azimuthal mean field. [Of course, the azimuthally averaged velocity is itself a nonlocally defined field, but once computed it has a local value at each point in 3D or 2D (r, θ) space.] Like in [33], we find that the two prescriptions give almost identical results. As is commonly done, we define a Shakura-Sunyaev α_{SS} by

$$\alpha_{SS} \equiv \frac{\langle w^{r\phi} \rangle}{\langle P_G + P_B \rangle}, \tag{18}$$

where P_G and P_B are the gas and magnetic pressure, respectively. The result, included in Fig. 4, closely resembles the left panel of Fig. 19 in [33], especially the dip at smaller r in the lower resolution results, which is a new check on the consistency of IllinoisGRMHD with the codes with spherical-polar grids. We also compute the Maxwell stress from the azimuthally averaged field $\bar{\boldsymbol{B}}$, using the same MHD formulas and in the azimuthally averaged comoving frame. This is found to provide a much lower stress except very near the black hole, indicating that most of the angular momentum transport in the bulk of the disk accomplished by the magnetic field is done so by the nonaxisymmetric field (the fluctuations, not the mean), a point also mentioned by Dhang *et al.* [19]. Of course, using an ideal MHD formula for the stress tensor is not quite appropriate for the azimuthally averaged field tensor, which includes the effect of $\boldsymbol{\Delta E}$, but this residual EMF is itself a measure of the prevalence of nonaxisymmetry in the field and so does not affect the conclusion.

Because of the difference between the local 3D and azimuthally averaged velocity fields ($\boldsymbol{v}$ vs $\bar{\boldsymbol{v}}$), there is also a mean Reynolds stress which can transport angular momentum. This is calculated in the frame comoving with the local azimuthally averaged velocity field: $t^{\hat{r}\hat{\phi}} = \overline{\rho h u^{\hat{r}} u^{\hat{\phi}}}$. (Note that the azimuthal mean velocity does not contribute, since if the field were axisymmetric, $u^{\hat{i}}$ would be zero in the frame comoving with the azimuthal average velocity.) This Reynolds component is lower than the full (primarily nonaxisymmetric) Maxwell component but still larger than the Maxwell stress of the mean field.

In addition to the shear-type stresses quantified by α_{SS}, there can be a pressurelike contribution to the stress tensor from the nonaxisymmetric Reynolds and Maxwell stresses. We define the turbulent pressure as

$$P_t \equiv \frac{1}{3} \Delta T^{ab} (g_{ab} + u_a u_b). \tag{19}$$

This is a very rough definition—applied instead to the stress-energy tensor of ideal MHD, it would give $P + b^2/6$, where $b^2 = b_a b^a$ and $\boldsymbol{b}$ is the magnetic field in the $\boldsymbol{u}$ frame. We find this pressure to be close to the magnetic pressure (of the full field), which even after saturation is about a factor of 10 lower than the gas pressure. (See Fig. 5, discussed below, which plots the associated energy densities.) Thus, although turbulence dominates the angular momentum transport, it is very subdominant in pressure effects (e.g., determining the disk height).

We also compute time- and angle-averaged energy densities in the disk. The magnetic energy density is $b^2/2$. The magnitude b will be considered a function of magnetic and velocity 3-vectors. For the full magnetic energy density, we use 3D local values: $b(\boldsymbol{B}, \boldsymbol{v})$. For the magnetic energy of mean field, we use the same formula (justified as above for stresses) using azimuthally averaged quantities: $b(\bar{\boldsymbol{B}}, \bar{\boldsymbol{v}})$. The internal energy density of the gas is $P/(\Gamma - 1)$.

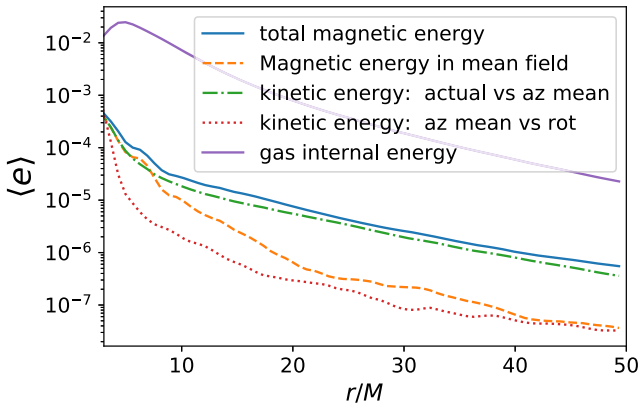

FIG. 5. Time- and angle-averaged energy densities within the disk as functions of r. See Eqs. (22)–(26) for definitions of each.

The kinetic energy of a fluid with 4-velocity $\boldsymbol{u}_1$ relative to a frame $\boldsymbol{u}_2$ can be defined as follows. Start from the Reynolds term in the fluid stress tensor $T^{ab}_R(\boldsymbol{u}_1) \equiv \rho h u^a_1 u^b_1$. The desired energy is in the $\boldsymbol{u}_2$ direction, so we must project $T^{ab}_R u_{2a}$. For an energy density, we must also specify a 4-velocity indicating the direction of flux of this energy we are considering; this is the frame in which the spatial integral converting energy density to energy would be performed. The natural choices are $\boldsymbol{u}_1$ (for comoving frame) and $\boldsymbol{n}$ (for regular spatial integration on the slice), and we choose the latter. The Reynolds energy density is then $u_{2a} n_b T^{ab}_R(\boldsymbol{u}_1) = -(\boldsymbol{u}_1 \cdot \boldsymbol{u}_2) W \rho h$. We then subtract off the rest contribution when $\boldsymbol{u}_1 = \boldsymbol{u}_2$ to get

$$e_K = -[(u_1 \cdot u_2) + 1] W \rho h, \tag{20}$$

$$e_K(\boldsymbol{v}_1, \boldsymbol{v}_2) = -[(u(\boldsymbol{v}_1) \cdot u(\boldsymbol{v}_2)) + 1] W \rho h, \tag{21}$$

where in the second line, we have (for convenience below) rewritten e_K as a function of 3-velocities, since a 4-velocity can be constructed from a 3-velocity by enforcing the normalization $\boldsymbol{u} \cdot \boldsymbol{u} = -1$.

There are three relevant 3-velocity fields in this problem: (1) $\boldsymbol{v}$, the 3D local velocity; (2) its azimuthal mean $\bar{\boldsymbol{v}}$; and (3) the rotational velocity $\bar{\boldsymbol{v}}_{\rm rot}$, which is $\bar{\boldsymbol{v}}$ with radial and meridional components removed. From each 3-velocity field, a 4-velocity field can be constructed by imposing the normalization $\boldsymbol{u} \cdot \boldsymbol{u} = -1$ [meaning that the t component of the azimuthal mean (az mean) 4-velocity is not exactly the azimuthal mean of the t component of the local 4-velocity]. We thus compute a turbulent kinetic energy density, comparing the 3D local velocity to the azimuthal average, and a rotational kinetic energy, comparing the azimuthal average velocity to the rotational velocity.

Thus, we define the following energy density averages, using the norm of Eq. (16):

$$\text{total magnetic energy} = \frac{1}{2}\langle b(\boldsymbol{B}, \boldsymbol{v})^2 \rangle \tag{22}$$

$$\text{total magnetic energy} = \frac{1}{2}\langle b(\bar{\boldsymbol{B}}, \bar{\boldsymbol{v}})^2 \rangle \tag{23}$$

$$\text{in mean field kinetic energy}: = \langle e_k(\boldsymbol{v}, \bar{\boldsymbol{v}}) \rangle \tag{24}$$

$$\text{actual vs az mean kinetic energy} = \langle e_K(\bar{\boldsymbol{v}}, \bar{\boldsymbol{v}}_{\rm rot}) \rangle \tag{25}$$

$$\text{az mean vs rot. gas internal energy} = \frac{1}{\Gamma - 1}\langle PW \rangle. \tag{26}$$

These energies are plotted in Fig. 5. We omit the rotational energy, which dominates all others, as would be expected for an accretion disk. The figure shows that the magnetic energy saturates more than an order of magnitude below the internal energy. However, the magnetic energy of the mean field saturates at a much lower value than this total magnetic energy. This indicates that the magnetic energy is mostly nonaxisymmetric ("turbulent"), and we infer that the energy in the turbulent magnetic field is close to the total magnetic energy. The kinetic energy from the difference of azimuthal mean vs actual velocities (the turbulent kinetic energy) dominates over the nonrotational kinetic energy from the mean field, indicating that inside the disk eddy motion dominates over mean poloidal motions. The total magnetic energy is seen to be very close to the turbulent kinetic energy, indicating that the kinetic and magnetic turbulent energies come into equipartition with each other. Recently, Aguilera-Miret *et al.* [43] have also found that the turbulent (i.e., nonaxisymmetric) components of magnetic and kinetic energy dominate in the disklike outer envelope of a binary neutron star postmerger remnant (but, interestingly, not in the core).

In Fig. 6, we plot the magnitude of the EMF, both the azimuthal mean $|\bar{E}|$ and the residuals $|\Delta E|$ and $|\Delta_3 E|$. We separate disk and jet regions. In the disk, the nonaxisymmetric component dominates except in the inner region. In the jet, the inner radii are strongly axisymmetric, and the outer radii are dominated by the lowest non-zero m modes.

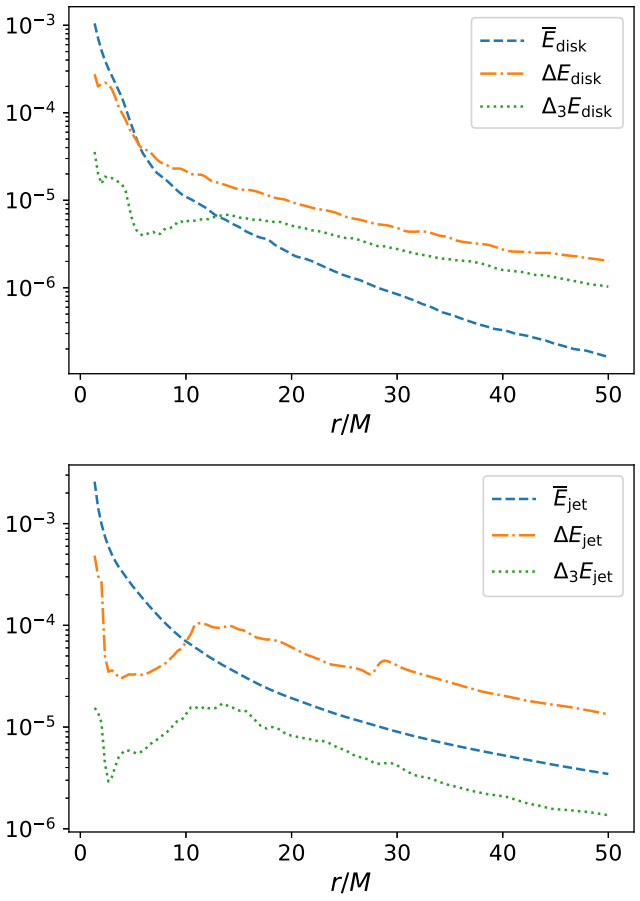

FIG. 6. Time- and angle-averaged vector magnitudes of EMFs inside the disk as functions of r. We compare the EMF of the mean fields with residual EMFs ΔE and $\Delta_3 E$.

IV. ISOTROPIC DYNAMO MODELS

A. Estimating an isotropic α effect

If one knows that the dynamo EMF is of an isotropic α form, extracting the pseudoscalar coefficient ($\alpha_{\rm dyn}$) becomes straightforward. Starting from the Newtonian formula $\boldsymbol{E} = \boldsymbol{B} \times \boldsymbol{v} + \alpha_{\rm dyn}\boldsymbol{B}$, one can take the dot product of both sides with respect to $\boldsymbol{B}$ to get $\alpha_{\rm dyn} = E \cdot B/B^2$. Remembering that $B^2 \gg E^2$ (see Fig. 1), we can recognize this as the ratio of the two Lorentz invariants of the electromagnetic field. We may, then, straightforwardly generalize the Newtonian formula as

$$\alpha_{\rm dyn} \equiv \frac{1}{2}\frac{\star F_{ab}F^{ab}}{F_{ab}F^{ab}}, \tag{27}$$

a pseudoscalar, as expected. Note that these are the invariants of the azimuthally averaged field tensors, not averages of the invariants of the field in 3D.

Because $\alpha_{\rm dyn}$ is expected to change sign across the equator, it would be inappropriate to compute an average over angles at a given radius or an average over the entire grid (unless one were to presume this parity and perform a sign flip in one hemisphere); it is better to average over time and radius to extract an average $\alpha_{\rm dyn}$ as a function of θ. This is plotted in Fig. 7.

A hemispherical average pseudoscalar $\alpha_{\rm dyn}$ had previously been extracted from a 3D disk simulation by Hogg and Reynolds [17]. They find $\alpha_{\rm dyn}$ in the range 1–2×10^{-4}. In magnitude, this is quite consistent with Fig. 7. There has been some disagreement over the sign of $\alpha_{\rm dyn}$, with some finding it positive in the upper hemisphere and some finding it negative (always with the other hemisphere being opposite sign). Our $\alpha_{\rm dyn}$ is negative in the Northern Hemisphere, consistent with [17,44,45]. Brandenburg and Donner [15] have suggested that this negative $\alpha_{\rm dyn}$, the opposite sign from classical dynamo theory, is an effect of shear in rotating twisted flux tubes.

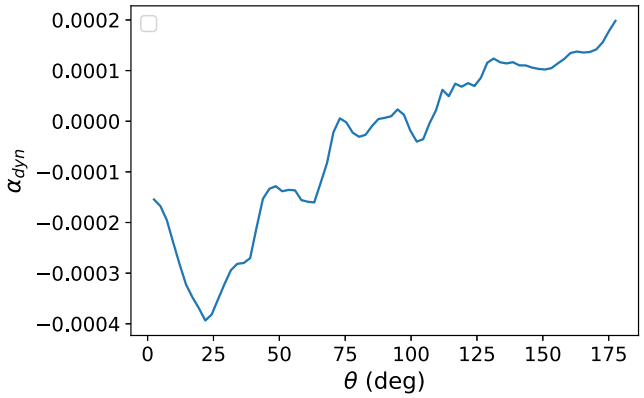

FIG. 7. Time- and radial-averaged $\alpha_{\rm dyn}$ [as defined by Eq. (27) vs θ].

B. Calibrating isotropic diffusivity effect with 2D MHD

To estimate an effective $\eta_{\rm dyn}$, we use the fact that the energy of $\bar{\boldsymbol{B}}$ inside the disk in the 3D simulation is smaller not only than the magnetic energy in the disk of the nonaveraged field in 3D, but also than the magnetic energy for a 2D MHD simulation of the same disk. One could say that the difference in energy is transferred from the mean field to the nonaxisymmetric field. Since this field is not captured by the fields tracked in a 2D simulation, it is in a sense equivalent to internal energy. The nonaxisymmetric effect that accomplishes this effective dissipative transfer thus acts as a diffusivity, and one can estimate an effective $\eta_{\rm dyn}$ by finding what level of resistivity is needed to reduce the disk magnetic energy to the same degree.

We wish to implement a version of Eq. (14) with $\alpha^i_j = \alpha_{\rm dyn}\delta^i_j$ and $\eta^i_j = \eta_{\rm dyn}\delta^i_j$ in a relativistic 2D MHD code. Such codes usually evolve the magnetic field 2-form (or, equivalently, the densitized magnetic field vector) ${}^2B_{ij} \equiv \epsilon_{ijk}B^k \equiv [ijk]\tilde{B}^k$.

Including an effective resistivity will introduce second spatial derivatives in the induction equation. We wish to obtain a spatially covariant equation while avoiding Christoffel symbols to the extent possible. Thus, we continue with form notation where possible, although the spatial metric necessarily will be invoked in Hodge duals and in creating the B-field 1-form ${}^1\boldsymbol{B} = B_a dx^a$. We introduce an EMF 1-form $\boldsymbol{R}$ to include all deviations from ideal MHD. Continuing in form notation, the dynamo-modified induction equation is

$$\partial_t {}^2\boldsymbol{B} = -\mathcal{L}_{\boldsymbol{v}} {}^2\boldsymbol{B} + d\boldsymbol{R}. \tag{28}$$

For the standard isotropic dynamo, $\boldsymbol{R}$ is

$$\boldsymbol{R}^{\rm dyn} = \alpha_{\rm dyn}{}^1\boldsymbol{B} + \eta_{\rm dyn}\star d{}^1\boldsymbol{B}, \tag{29}$$

where in fact we use ${}^u\boldsymbol{B}$ as defined in Eq. (12) for the magnetic field. In components,

$$R^{\rm dyn}_k = \alpha_{\rm dyn}B_k + \eta_{\rm dyn}\frac{1}{2}\epsilon_{ijk}A^{ij}, \tag{30}$$

$$\begin{aligned} A^{ij} &= \gamma^{i\ell}\gamma^{jm}(\nabla_\ell B_m - \nabla_m B_\ell) \\ &= \gamma^{i\ell}\gamma^{jm}(\partial_\ell B_m - \partial_m B_\ell) \end{aligned} \tag{31}$$

(i.e., by using exterior derivatives, we avoid covariant derivatives). In order to avoid the time step limitations of explicitly evolving a parabolic system, we promote R_k to an evolution variable driven to its dynamo form,

$$\partial_t R_k = \tau^{-1}_{\rm drive}(R^{\rm dyn}_k - R_k). \tag{32}$$

We set $\tau^{-1}_{\rm drive} = \hat{\tau}_d\Omega_K$, where Ω_K is the Keplerian angular frequency; we report results for $\hat{\tau}_d = 0.5$ but have checked that the behavior of all quantities is insensitive to it within a wide range. Smaller $\tau_{\rm drive}$ will force R_k to track $R^{\rm dyn}_k$ more

closely, but we wish to keep $\eta_{\rm dyn}/\tau_{\rm drive} < 1$ to avoid acausal propagation speeds.

The coefficient $\eta_{\rm dyn}$ is set to $c_s\ell$, where ℓ is an effective mixing length; it is natural to suppose that it is similar in magnitude to the mixing length used to set the α effective viscosity. This similarity is confirmed for shearing box studies (more precisely, that the turbulent magnetic Prandtl number is roughly unity [46–48]), but it should be remembered that the distinction between mean and turbulent field is different in these studies, so their applicability to azimuthally averaged dynamics cannot be certain. We set

$$\ell = \alpha_\eta c_s \Omega_K^{-1} f_\rho f_\beta f_{\rm BH}, \tag{33}$$

where α_η is a free constant (the symbol "α" chosen for its analogy to $\alpha_{\rm SS}$, not to $\alpha_{\rm dyn}$), and the factors $f_\rho = \rho/(\rho + 10^{-4}\rho_{\rm init,max})$, $f_\beta = P_{\rm gas}/(P_B + P_{\rm gas})$, $f_{\rm BH} = \max[0, 1-(r/3M)^{-2}]$ suppress resistivity in the low-density region, the magnetosphere, and near the horizon, respectively.

We implement the above in the HARMPI code, a version of the GRMHD code HARMPI [24,25] publicly available at GitHub [49]. Note that, unlike truly 4D covariant resistive MHD codes, we do not evolve the actual electric field, although making $\boldsymbol{R}$ an evolution variable arguably accomplishes something similar. Our less-precise implementation does have the advantage that no problem of stiffness arises in the limit of low $\eta_{\rm dyn}$.

In Fig. 8, we show the magnetic energy in the disk as a function of time for several simulations. For the 3D simulation, we plot both total magnetic energy and the (much smaller) magnetic energy of the mean field. We also show HARMPI in 2D with ideal MHD, which produces a magnetic energy far too high during the evolution period to match the mean of the 3D field. Better agreement can be achieved by adding an isotropic dynamo η term with $\alpha_\eta = 0.018$.

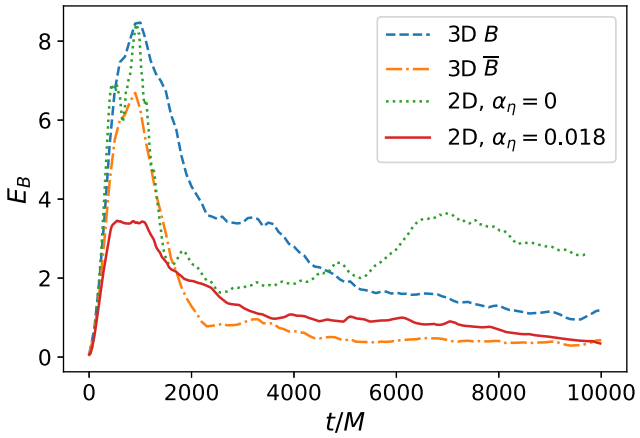

FIG. 8. Total magnetic energies in the disk vs time. For the 3D run, we show total magnetic energy and magnetic energy in the mean field. For 2D runs, we show runs with two different values of the effective resistivity parameter α_η [see Eq. (33)].

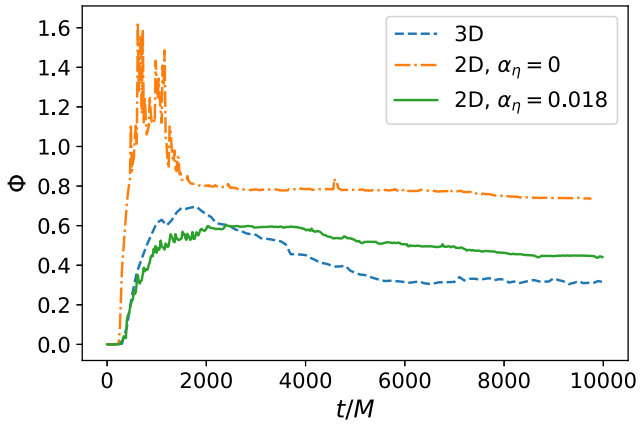

FIG. 9. Horizon fluxes vs time for the same runs as in Fig. 8.

In Fig. 9, we plot magnetic flux $\Phi \equiv \int |B^r| dA$ on the horizon. For electromagnetic energy extraction and jet formation, it is important that suppressing the disk magnetic energy does not also suppress the horizon flux. Our implementation of η does not add resistivity outside the high-density region or near the horizon, and we do see that the $\alpha_\eta = 0.018$ run maintains a horizon flux that is fairly constant and similar to 2D. It remains to be seen how it would fare for longer timescales (not pursued for this project for lack of a 3D comparison) and whether the polar field, which eventually diminishes in 2D, needs to be replenished by a slight α effect. Furthermore, it is a separate challenge to show that, for a more extended magnetized disk (e.g., the more common magnetically arrested disk test disks [50]), magnetic flux could, over an extended period of time, accurately survive while advecting onto the horizon.

V. NONISOTROPIC DYNAMO MODELS

We now attempt to extract α^i_j and η^i_j by linear least-squares fitting. Suppose one attempts a fit using N data points, each data point corresponding to one event—a particular spatial location at a particular time. At each data point, there are three equations, one for each component ΔE^i. For a given component i, combining all data points, we have the matrix equation that we wish to be satisfied

$$\boldsymbol{y}_i \cong \boldsymbol{A}_i \cdot \boldsymbol{x}_i, \tag{34}$$

where $\boldsymbol{y}_i$ is length-N column vector made of all the ΔE^i, $\boldsymbol{x}_i$ is a six-dimension column vector made of the α^i_j and η^i_j $\forall$ j, and $\boldsymbol{A}_i$ is a $N \times 6$ matrix made of B^j and J^j $\forall$ j. We use the symbol "$\cong$" to mean that this is an equation deviation from which will be minimized (but, since there are more conditions than variables, will not be exactly satisfied). The best-fit model is a particular $\boldsymbol{x}_i = \boldsymbol{x}_i^{\rm fit}$.

In choosing a residual function to be minimized, one must decide how data points are weighted. One natural choice is to treat the absolute error at all points as equally important and minimize $(\boldsymbol{y}_i - \boldsymbol{A}_i \cdot \boldsymbol{x}_i^{\rm fit})^T(\boldsymbol{y}_i - \boldsymbol{A}_i \cdot \boldsymbol{x}_i^{\rm fit})$. This will have the effect that the fit will care more to reduce relative error at points with strong field and high ΔE^i. Alternatively, one might wish to weight relative errors at each point similarly. One can do this by normalizing $\boldsymbol{A}$ and $\boldsymbol{y}$ at each spacetime event P used in the fit, dividing all components of each by $||y||_P$, the L2 norm of the elements of $\boldsymbol{y}$,

$$||y||_P = \sqrt{\frac{1}{3}\sum_{i=1}^{3} y_i^2(P)}. \tag{35}$$

It is not obvious which sort of weighting is more desirable, so we have experimented with both. For runs with weighting, we wish to avoid the possibility of fits dominated by attempts to reduce relative error in unimportant weakly magnetized, very low-EMF regions. Therefore, for these fits, we multiply $\boldsymbol{A}$ and $\boldsymbol{y}$ at each event P by the weighting factor

$$w_P = \max(||y||_P, 10^{-3} y_{\rm max})^{-1}, \tag{36}$$

where $||y||_P$ is the L2 norm $||y||$ at P, and $y_{\rm max}$ is the maximum value of $||y||_P$ across all P used for the given fit (i.e., the L∞ norm across events of the L2 norm at each event).

A. Model validation

One measure of model accuracy is how well the model matches the original data. We compute this accuracy by the following measure:

$$\chi_i^2 \equiv \frac{(\boldsymbol{y}_i - \boldsymbol{A}_i \cdot \boldsymbol{x}_i^{\rm fit})^T(\boldsymbol{y}_i - \boldsymbol{A}_i \cdot \boldsymbol{x}_i^{\rm fit})}{\boldsymbol{y}^T\boldsymbol{y}}. \tag{37}$$

This is related to the usual χ-squared statistic but with a different normalization. More commonly, χ^2 is normalized by the expected error, so that its magnitude for a good fit is unity. In this case, we normalize by the data itself, so a very good fit would have $\chi^2 \ll 1$. This is probably unrealistic for a turbulent system, so we set our criterion for fit to be $\chi^2 < 0.5$. In a study of subgrid models of MHD turbulence, Viganò *et al.* [12] consider an alternate accuracy measure, the Pearson correlation coefficient between the data and the best fit. They do not find it to be a useful accuracy indicator, and we have not measured it.

We also measure the variance, which provides the uncertainty in the best-fit values $\boldsymbol{x}_i^{\rm fit}$. A variance estimate is provided by the SVD composition, valid for Gaussian statistics and uncorrelated data points. In fact, even for the staggering in space and time we use to mitigate correlations, data points remain significantly correlated, so Bendre *et al.* [18] find (and we confirm) that the Gaussian variance significantly underestimates the uncertainty in $\boldsymbol{x}_i^{\rm fit}$.

Instead, we estimate variance, similar to Bendre *et al.*, by computing $\boldsymbol{x}_i^{\rm fit}$ restricting the data used to different subsets of time steps. In our case, we compute $\boldsymbol{x}_i^{\rm fit}$ for even time steps ($\boldsymbol{x}_{\rm even}$), for odd time steps ($\boldsymbol{x}_{\rm odd}$), and for all time steps ($\boldsymbol{x}_{\rm all}$). Between two fits, $\boldsymbol{x}^A$ and $\boldsymbol{x}^B$, define relative difference for each component i of $\boldsymbol{x}$ as $\delta_i^{A,B} \equiv (x_i^A - x_i^B)^2/(x_i^A + x_i^B)^2$. For each i, we get an overall δ_i by taking the maximum of $\delta_i^{\rm even,odd}$, $\delta_i^{\rm even,all}$, and $\delta_i^{\rm odd,all}$. For the fit to have some value, there must be at least one component of $\boldsymbol{x}^{\rm fit}$ that is consistent across fits (and this will probably be the one that contributes most to the fit), so for our overall variance measure, we minimize over components i,

$$\mathrm{var}(\boldsymbol{x}) = \min_i[\max(\delta_i^{\rm even,odd}, \delta_i^{\rm even,all}, \delta_i^{\rm odd,all})]. \tag{38}$$

Some fits involve more than one point in space, so for models 2 and 4 below we also compute variances by skipping even and odd points in r and (if it varies within the fit) θ. Then for each x_i component we maximize over relative differences for different time and space samples before extracting the best-constrained component.

This is a very generous measure, since we only require one dynamo coefficient to be well constrained. For the model parameters to be meaningful, we require $\mathrm{var}([\boldsymbol{x}]) < 0.3$.

Note that the more global the model, the more data points are relevant per fitting parameter. This will tend to reduce variance, since one has very good statistics, but it is more difficult to have acceptable χ^2, since the model must work well for more points. Conversely, for more local models, χ^2 will likely become smaller, but one should not be too encouraged by this, because one can fit anything as the number of conditions drops toward the number of fitting parameters, and the tendency to overfit will often be revealed in a high variance.

B. Pointwise models

We attempt two models for which α_j^i and η_j^i are taken to be functions of spatial coordinates but independent of time. In model 1, they are taken to be functions of r and θ, i.e., there is an independent fitting procedure applied at each point. This is similar to the model construction of Dhang *et al.* [19]. In model 2, we take the dynamo coefficients to be functions of θ, i.e., they are presumed to be constant in both r and t. Thus, compared to model 1, each fit in model 2 involves more data (corresponding to multiple points along a radial ray), which will tend to result in better variance but worse χ^2. We perform fits both with and without weighting, meaning equations at data points are weighted either with the factor 1 or the factor w in Eq. (36).

TABLE I. Fit quality measures for models 1 and 2.

Model	Region	Weighting	χ^2	Var
1	Disk	1	0.599	0.789
	Disk	w	0.776	0.834
	Jet	1	0.483	0.532
	Jet	w	0.747	0.781
2	Disk	1	0.899	0.418
	Disk	w	0.938	0.355
	Jet	1	0.985	0.206
	Jet	w	0.969	0.328

Results for model validation are shown in Table I. For presenting average variance (Var) and χ^2, we divide the space into two regions: "jet" for the region within $\pi/3$ of the axis, and "disk" for all other latitudes. As we see, none of the models are very good by either of our validation measures.

C. Global models

We now attempt to fit to a model for which α^{ij} and η^{ij} are not explicit functions of spatial coordinates.

For a covariant model, we would also have to build fitting formulas for these tensors out of physically relevant vectors and tensors, e.g., the metric γ^{ij} or the velocity v^i. Since α^{ij} is axial, we require at least one pseudoscalar or pseudovector ingredient. The construction of an azimuthally averaged system only makes sense if an approximate azimuthal Killing vector $\boldsymbol{e_\phi} = \partial/\partial\phi$ has been identified. We can, thus, assume its availability and expect that it may appear in the formulas for dynamo tensors, both because of its physical relevance (as roughly the direction of mean velocity) and its relevance in constructing the 2D system (which breaks 3D rotational invariance). We will use the normalized vector

$$\hat{\boldsymbol{e}}_{\boldsymbol{\phi}} \equiv (g_{\phi\phi})^{-1/2}\frac{\partial}{\partial\phi}. \tag{39}$$

We get a pseudovector, corresponding to the direction of the symmetry axis, by taking a curl

$$\zeta^i \equiv \epsilon^{ijk}\nabla_j(e_\phi)_k = \epsilon^{ijk}\partial_j(e_\phi)_k. \tag{40}$$

We will use the normalized version $\hat{\boldsymbol{\zeta}} \equiv \boldsymbol{\zeta}/|\zeta|$, which resembles the Cartesian z direction.

Some dynamo models also use $\nabla\rho$, the gradient of the density, or they use a gradient of the turbulent velocity (assuming some knowledge of this) [44]. For a thin accretion disk, the direction of density gradient would be close to $\mathrm{sign}(z)\hat{\boldsymbol{\zeta}}$ except on the equator. To build the expected parity factor in $\alpha_{\rm dyn}$ (something like $\cos\theta$), we instead want a nearly radial third vector, which could be interpreted as the direction of gravity. Since we have already assumed an approximate timelike Killing vector is available to us, $\boldsymbol{e_t}$, we might as well use it to define this direction

$$\boldsymbol{f} \equiv -\nabla(e_t\cdot e_t) = -\nabla g_{tt}, \tag{41}$$

$$\hat{\boldsymbol{f}} \equiv \boldsymbol{f}/|f|. \tag{42}$$

This then provides the pseudoscalar $\mu \equiv \hat{f}\cdot\hat{\zeta}$, which is close to $\cos\theta$. The resulting triad $\{\hat{\boldsymbol{\phi}},\hat{\boldsymbol{\omega}},\hat{\boldsymbol{f}}\}$ provides a suitable vector basis inside the disk. For global models including the polar region, it is not usable because on the poles $\hat{\boldsymbol{\omega}}$ and $\hat{\boldsymbol{f}}$ are parallel or antiparallel. We can alternatively use the azimuthal Killing vector to define

$$\boldsymbol{\varpi} \equiv -\nabla(e_\phi\cdot e_\phi) = -\nabla g_{\phi\phi}, \tag{43}$$

$$\hat{\boldsymbol{\varpi}} \equiv \boldsymbol{\varpi}/|\varpi|. \tag{44}$$

Thus, $\hat{\boldsymbol{f}}$ resembles the spherical-polar radial direction and is used to define the pseudoscalar μ, while $\hat{\boldsymbol{\varpi}}$ resembles cylindrical-polar radial direction and is used as a basis vector.

We then have a triad of normalized but not orthogonal vectors in $\hat{\boldsymbol{e}}_{\boldsymbol{\phi}}$, $\hat{\boldsymbol{\zeta}}$, and $\hat{\boldsymbol{\varpi}}$ (and an associated dual cobasis); we denote components in this basis by hatted capital Latin letters, e.g., $B_{\hat{I}} = B\cdot e_{\hat{I}}$.

The global dynamo model is a tensor equation for constructing the residual EMF $\boldsymbol{\Delta E}$ in terms of the magnetic field $\boldsymbol{B}$, an axial vector, and some polar vector $\boldsymbol{Z}$, which we choose to be either $\boldsymbol{J} \equiv \boldsymbol{\nabla}\times\boldsymbol{B}$ or $B^2\boldsymbol{v}_T$, where $\boldsymbol{v}_T$ is the transport velocity of the fluid. For $\boldsymbol{B}$, we report results using ${}^u\boldsymbol{B}$ (and its curl for $\boldsymbol{J}$), although we have also tried using the normal frame $\boldsymbol{B}$ with similar results.

The tensor equation is

$$\Delta E^{\hat{I}} = \alpha^{\hat{I}\hat{K}}B_{\hat{K}} + \eta^{\hat{I}\hat{K}}Z_{\hat{K}}, \tag{45}$$

$$\alpha^{\hat{I}\hat{K}}(\boldsymbol{x},t) = a^{\hat{I}\hat{K}}\mu^{n_a(\hat{I},\hat{J})}\psi(\boldsymbol{x},t), \tag{46}$$

$$\eta^{\hat{I}\hat{K}}(\boldsymbol{x},t) = e^{\hat{I}\hat{K}}\mu^{n_e(\hat{I},\hat{J})}\psi(\boldsymbol{x},t), \tag{47}$$

where $n_a(\hat{I},\hat{J})$ and $n_e(\hat{I},\hat{J})$ are either 0 or 1, whichever is needed to obtain consistent parity for all terms.

The scalar function $\psi(\boldsymbol{x},t)$ can be any scalar function constructed from the dynamical variables, with variables expected to be correlated with $\boldsymbol{\Delta E}$ being attractive choices. Below, we consider several choices, including unity and the 2D spatial shear scalar $\sigma = (\sigma_{IJ}\sigma^{IJ})^{1/2}$. We have also tried the gradient of the angular velocity $|\nabla\Omega|$ (this is related to the vorticity, which could affect dynamo coefficients [15]), the sound speed c_s, and the fraction of the pressure that is gas or magnetic [i.e. $P_G/(P_G+P_B)$ and $P_B/(P_G+P_B)$]. We also try the scalar rms deviation of $\boldsymbol{B}$ and of $\boldsymbol{v}_T$ from their azimuthal average, e.g.,

$$B_{\rm rms} = [\overline{|B-\bar{B}|^2}]^{1/2}. \tag{48}$$

In an actual 2D simulation, these functions would not be available. Rather, new evolution variables would have to be introduced with evolution equations designed to suitably approximate them. However, designing such dynamics is only a worthwhile exercise if it is found that the actual rms measures of nonaxisymmetry provide useful $\psi(\boldsymbol{x},t)$ variables. For all of the candidate $\psi(\boldsymbol{x},t)$, we have checked the Pearson correlation coefficient between that ψ and the magnitude ratio $|\boldsymbol{\Delta E}|/|\boldsymbol{B}|$. No ψ yielded strong correlations, but this might be because of the other variables in Eqs. (45)–(47).

We also consider two alternatives for what constitutes the EMF residual: $\boldsymbol{\Delta E}$ and $\Delta_m \boldsymbol{E}$.

We produce two types of global models. For model 3, we use data across all r, θ, and t to produce a single fit for the *numbers* $\alpha^{\hat{I}\hat{K}}$, $\eta^{\hat{I}\hat{K}}$. For model 4, we use the time average of the data and fit for the numbers $\alpha^{\hat{I}\hat{K}}$, $\eta^{\hat{I}\hat{K}}$ using points across all r, θ. Model 4 can be thought of as a low-pass filter in time, and it is most sensible to smooth only over timescales less than the dynamo cycle period. In using all of our time slices, we take advantage of the (otherwise unfortunate) fact that we do not evolve for multiple cycles.

We introduce a couple of variations. First, it is possible that the dynamics is very different in the jet and disk regions, so we create fits using data only within certain latitude regions. For this purpose, disk is defined as the region between $\pi/3 < \theta < 2\pi/3$ and jet is defined as the regions $\theta < \pi/5$ and $\theta > 4\pi/5$, so the intermediate coronal region is excluded from both. This division is slightly different from the disk and jet designations for reporting model 1 and 2 quality measures in Table I, but the separation here plays a different role. It is used to determine which data are used for creating a given fit, rather than just which region is being averaged over for reporting a given norm after fitting is completed.

Also, one could argue that a dynamo model need not capture small-scale features of $\Delta E^{\hat{I}}$, so in some cases we try smoothing data before fitting. This effectively reduces the amount of independent data and can be expected to give higher χ^2. We convolve the data with a smoothing kernel, here chosen to be a triangle function in each direction centered on the point. Specifically, if the half-length of the triangle is $N_{\rm sm}$ points, then variable f at point i, j (indexing location in r and θ, respectively) is smoothed as follows:

$$f_{i,j} \to \sum_{m=-N_{\rm sm}}^{N_{\rm sm}} \sum_{n=-N_{\rm sm}}^{N_{\rm sm}} \frac{w_{mn}}{\mathcal{Z}} f_{i+m,j+n}, \tag{49}$$

$$w_{mn} = \left(1 - \frac{|m|}{N_{\rm sm}+1}\right)\left(1 - \frac{|n|}{N_{\rm sm}+1}\right), \tag{50}$$

TABLE II. Fit quality measures for models 3 and 4.

Model	Region	$\boldsymbol{Z}$	w	m_t	ψ	$N_{\rm sm}$	χ^2	Var
3	All	J	1	0	1	3	0.975	0.0068
		v	1	0	1	3	0.970	0.018
		J	1	0	$v_{\rm rms}$	3	0.664	0.001 24
		J	1	0	σ	3	1.000	0.001
		J	1	3	1	3	0.996	0.006 52
		J	1	3	$v_{\rm rms}$	3	0.980	0.001 03
		v	1	3	$v_{\rm rms}$	3	0.978	0.001 03
		J	w	0	1	3	0.992	0.057
		v	w	0	1	3	0.970	0.054
4	Jet	J	1	0	1	3	0.797	0.000 96
	Jet	v	1	0	1	3	0.549	0.0082
	Disk	J	1	0	1	3	0.427	0.002 85
	Disk	v	1	0	1	3	0.473	0.0004
	All	J	1	0	1	3	0.854	0.0027
		v	1	0	1	3	0.600	0.001
		J	1	0	1	0	0.934	0.008
		J	1	0	1	6	0.741	0.001
		J	1	0	σ	3	0.934	0.0145
		J	1	0	$v_{\rm rms}$	3	0.685	0.001
		J	1	0	$B_{\rm rms}$	3	0.966	0.008
		J	w	0	1	3	0.922	0.001
		J	1	3	1	3	0.934	0.001
		J	1	3	$B_{\rm rms}$	3	0.968	0.008
		v	1	3	1	3	0.611	0.001
		J	1	3	$v_{\rm rms}$	3	0.771	0.001

$$\mathcal{Z} = \sum_{m=-N_{\rm sm}}^{N_{\rm sm}} \sum_{n=-N_{\rm sm}}^{N_{\rm sm}} w_{mn}. \tag{51}$$

Thus, data at each point are replaced by a weighted sum of its neighbors, and the amount of smoothing is determined by the half-length of the triangle, $N_{\rm sm}$.

Quality of fit measures are reported in Table II. Because of the large number of events used to fit a small number of global parameters, best-fit values to at least some dynamo coefficients can now be determined precisely. However, χ^2 reveals that none of these best fits are good matches for the data, at least not good enough according to our criteria for viability. We see many cases with χ^2 close to 1, which occurs because the functions $\boldsymbol{B}$ and $\boldsymbol{Z}$ do not well overlap with $\boldsymbol{E}$ (see Figs. 1 and 2), and none of our chosen correlates ψ successfully corrects for this, so the best fit is obtained by making the model values $\boldsymbol{A}\cdot\boldsymbol{x}^{\rm fit}$ small compared to the data $\boldsymbol{y}$.

VI. SUMMARY

In this paper, we have considered how to perform 2D simulations of a turbulent, magnetized accretion disk such that the results best resemble the azimuthal average of 3D simulations of the same system. This requires the feedback of the (not captured) nonaxisymmetric turbulence on the

azimuthal mean fields (in the form of effective stresses and dynamo terms) be related by closure conditions to the known mean fields.

A. New analyses

Notably new analysis tools introduced in this paper include the following.

(i) Relativistic definitions of nonaxisymmetric features: We introduce a new definition of kinetic energy given two velocity flows [Eq. (20)]. We introduce a definition of the dynamo α parameter in terms of Lorentz invariants of the azimuthally averaged Faraday tensor [Eq. (27)]. Turbulent diffusivity was estimated by comparing disk magnetic energy for azimuthally averaged 3D evolution vs resistive 2D evolution.

(ii) A new implementation of resistive GRMHD: In the spirit of spatially covariant large-eddy models of momentum transport, which have proven useful in numerical relativity, we introduce a new formulation of turbulent resistivity which is spatially covariant but much simpler than a full, 4D covariant resistive MHD and does not become stiff or require implicit time stepping.

(iii) New variations of the dynamo closure condition: We perform least-squares fits of the data to a number of new variations of the dynamo closure condition, as summarized below.

B. Main results

Our main results are the following.

(i) Dominance of the turbulent field: To properly understand this task, it must be clearly understood that inside the disk the uncaptured turbulent components of $\boldsymbol{B}$ dominate over their azimuthally averaged values, and this is also true of $\boldsymbol{\mathcal{V}}$ (excepting the overall rotation). We quantified this in several ways. First, the magnetic energy of the averaged magnetic field is an order of magnitude lower than the actual magnetic energy. Similarly, the kinetic energy associated with the difference between the averaged and actual velocity is an order of magnitude larger than the kinetic energy associated with the nonrotational piece of the averaged velocity. Also, the $r\phi$ stress associated with transport of angular momentum inside the disk is dominated by Maxwell stress from the nonaxisymmetric field, and even the Reynolds stress of nonaxisymmetric flow dominates over the Maxwell stress of the averaged magnetic field. Thus, it is incorrect to imagine that 2D GRMHD simulations can dispense with the effective viscosity of 2D hydrodynamic disk simulations. Finally, the EMF in the disk is dominated by contribution from the nonaxisymmetric components, except in the very inner region. Note that these conclusions do not hold in the polar regions, where there is a significant axisymmetric component due to the jet.

(ii) Overall magnitude of dynamo terms: We suggest ways of estimating the overall magnitude of the dynamo tensors α^i_j and η^i_j for a given 3D simulation. These methods have the defect that they assume isotropic forms of the tensors and the assumption involved in estimating each ignores the effect of the other, but they do provide values consistent with expectations from previous studies. Namely, the isotropic $\alpha_{\rm dyn}$ has a magnitude of 10^{-4}, with the sign being different in each hemisphere. (There is dispute in the literature on which sign goes with which hemisphere; we find $\alpha_{\rm dyn} < 0$ in the Northern Hemisphere.) Our technique for estimating $\eta_{\rm dyn}$ (matching resistive 2D GRMHD to averaged ideal 3D GRMHD) confirms that the turbulent magnetic Prandtl number is of order 1.

(iii) The failure of standard closure models: We tested closure models for the residual EMF $\boldsymbol{\Delta E}$ via least-squares fitting. A model was considered acceptable only if the difference between the data and the model was small relative to the magnitude of the data ("small" defined as "less than 50%") and at least one dynamo tensor component is well constrained (meaning known to within 30%). Even by these generous criteria, the following models fail.
   (a) $\boldsymbol{\Delta E}$ as linear functions of $\boldsymbol{B}$ and $\boldsymbol{J}$, with the fitting coefficients allowed to be functions of space but not time.
   (b) $\boldsymbol{\Delta E}$ as linear functions of $\boldsymbol{B}$ and $\boldsymbol{J}$, with the fitting coefficients allowed to be functions only of angle but not time or radius.
   (c) $\boldsymbol{\Delta E}$ as linear functions of $\boldsymbol{B}$ and $\boldsymbol{J}$ multiplied by some scalar function of variables available to the 2D mean system, where the fitting coefficients are global, i.e., not functions of space or time.
   (d) The same as above, but with $\boldsymbol{\Delta E}$, $\boldsymbol{B}$, $\boldsymbol{J}$, and the various scalar functions averaged over time, so that a fit was only attempted for the time average of $\boldsymbol{\Delta E}$ in terms of other time averages.

(iv) The failure of closure model variations: We also test generalizations of the standard closure model, all of which seem *a priori* quite promising but none of which, to our knowledge, have been attempted before. Nevertheless, these also fail to produce acceptable models.
   (a) $\boldsymbol{\Delta E}$ as linear functions of $\boldsymbol{B}$ and $\boldsymbol{\mathcal{V}}$ (instead of $\boldsymbol{J}$), again multiplied by some scalar in the 2D evolution.
   (b) Global models allowing proportionality scalars representing the magnetic or kinetic energy of rms deviation of the fields from their azimuthal mean.

(c) Global models for $\mathbf{\Delta_3 E}$, the EMF left over when one removes not only the azimuthal average but also all $m \leq 3$ contribution, rather than $\mathbf{\Delta E}$.

VII. CONCLUSIONS

Modeling nonaxisymmetric effects in accretion disks is challenging because, for some quantities of interest, the nonaxisymmetric/fluctuating part dominates over the axisymmetric/mean part. Inside the disk, the mean field is often itself more like residual noise than a dominant field component, and it is not surprising that nonaxisymmetric effects cannot be easily correlated to its local values.

One crucial feedback effect of fluctuations onto the mean structure is the angular momentum transport, often captured via viscous hydrodynamics. Mean fields remain important in the polar region, and for the long-term maintenance and evolution of this region, and for the late-time oscillating toroidal mean field, 2D models will need to model the mean field while incorporating nonaxisymmetric effects. Using results for a 3D Cartesian FMR GRMHD code, we have quantified these feedbacks: the momentum transport $\alpha_{\rm SS}$ and the effective dynamo coefficients $\alpha_{\rm dyn}$ and $\eta_{\rm dyn}$, finding reasonable magnitudes for all. We then tested whether linear closure models can provide a good fit to the residual EMF, considering a wide range of pointwise and global models of growing complexity. None of these provided satisfactory models.

We then considered variations on the standard linear closure. Some of these would require significant effort to implement, so it is important to test beforehand whether they even in principle provide viable models. In particular, designing evolution equations for $B_{\rm rms}$ or $v_{\rm rms}$ does not seem promising because we have failed to find a way to use them effectively, even if the exact instantaneous rms values are provided to aid dynamo fits. Nor did we find $\mathbf{\Delta_3 E}$ easier to fit to mean variables than $\mathbf{\Delta E}$, although, of course, evolving $m = 1$ to $m = 3$ modes of all variables would capture a significant fraction of the nonaxisymmetric effects in itself even without a closure for $\mathbf{\Delta_3 E}$, at the cost of being a low-azimuthal resolution 3D model rather than a 2D model. More general and sophisticated models could still be attempted, e.g., providing evolution equations for $\mathbf{\Delta E}$ itself, analogous to turbulence models that evolve the Reynolds stress.

On the other hand, this is a stricter test than what is required of viscous hydrodynamics, in that it is usually not considered necessary to show that the residual stress tensor is well fitted by a viscous stress tensor with some kinematic viscosity that is either a constant or is some specified function of azimuthal mean variables. Rather, one insists that the viscosity capture one particular effect and calibrate a coefficient setting ν so that one effect has the appropriate magnitude. Similarly, if one identifies the key features needed for long-term evolution, e.g., reducing poloidal field strength in the disk while maintaining it in the poles, simple models can be calibrated to do this.

The main interest of this study is to have explored some new ways of quantifying dynamo effects in 3D simulations. The main limitation of this study is the narrowness of the data to which it has been applied. More could be learned by carrying out a similar analysis on a run that continues much longer for multiple dynamo cycles. It is also necessary to run with different accretion disk–black hole configurations: disks around lower-spinning black holes, different seed fields (e.g., toroidal), larger disks, disks that become magnetically arrested within a reasonable evolution time, radiatively efficient disks.

ACKNOWLEDGMENTS

We acknowledge S. Bose, M. Forbes, F. Foucart, F. H. Nouri, and E. Most for useful conversations and encouragement, and we express deep gratitude to A. Tchekhovskoy for making the HARMPI code publicly available. M. D. D. gratefully acknowledges support from the NSF through Grants No. PHY-2110287 and No. PHY-2407726 and support from NASA through Grant No. 80NSSC22K0719. Z. B. E. gratefully acknowledges support from NSF Awards No. AST-2227080, No. OAC-2227105, No. PHY-2110352, and No. PHY-2409654, as well as NASA Awards No. ISFM-80NSSC21K1179 and No. TCAN-80NSSC24K0100. B. K. gratefully acknowledges support from NASA LISA Preparatory Science Award No. 80NSSC24K0360; this material is also based upon work supported by NASA under Award No. 80GSFC21M0002. Computational resources for performing the GRMHD simulations were provided by the WVU Research Computing Thorny Flat HPC cluster, which is funded in part by NSF OAC-1726534. Postsimulation analysis was performed in part on the Pleiades cluster at the Ames Research Center, with support provided by the NASA High-End Computing (HEC) Program.

DATA AVAILABILITY

The data that support the findings of this article are not publicly available because no suitable repository exists for hosting data in this field of study. The data are available from the authors upon reasonable request.

[1] G. K. Batchelor, Computation of the energy spectrum in homogeneous two-dimensional turbulence, Phys. Fluids **12**, II-233 (1969).

[2] P. A. Davidson, *Turbulence: An Introduction for Scientists and Engineers* (Oxford University Press, New York, 2015).

[3] T. G. Cowling, The magnetic field of sunspots, Mon. Not. R. Astron. Soc. **94**, 39 (1933).

[4] H. K. Moffatt, *Magnetic Field Generation in Electrically Conducting Fluids* (Cambridge University Press, Cambridge, England, 1978).

[5] A. Brandenburg and K. Subramanian, Astrophysical magnetic fields and nonlinear dynamo theory, Phys. Rep. **417**, 1 (2005).

[6] A. Sadowski, R. Narayan, A. Tchekhovskoy, D. Abarca, Y. Zhu, and J. C. McKinney, Global simulations of axisymmetric radiative black hole accretion discs in general relativity with a mean-field magnetic dynamo, Mon. Not. R. Astron. Soc. **447**, 49 (2015).

[7] M. Bugli, L. Del Zanna, and N. Bucciantini, Dynamo action in thick disks around Kerr black holes: High-order resistive GRMHD simulations, Int. J. Mod. Phys. Conf. Ser. **28**, 0203 (2014).

[8] N. Tomei, L. Del Zanna, M. Bugli, and N. Bucciantini, General relativistic magnetohydrodynamic dynamo in thick accretion discs: Fully non-linear simulations, Mon. Not. R. Astron. Soc. **491**, 2346 (2020).

[9] C. Vourellis and C. Fendt, Relativistic outflows from a GRMHD mean-field disk dynamo, Astrophys. J. **911**, 85 (2021).

[10] M. Shibata, S. Fujibayashi, and Y. Sekiguchi, Long-term evolution of neutron-star merger remnants in general relativistic resistive magnetohydrodynamics with a mean-field dynamo term, Phys. Rev. D **104**, 063026 (2021).

[11] B. Giacomazzo, J. Zrake, P. Duffell, A. I. MacFadyen, and R. Perna, Producing magnetar magnetic fields in the merger of binary neutron stars, Astrophys. J. **809**, 39 (2015).

[12] D. Viganò, R. Aguilera-Miret, and C. Palenzuela, Extension of the subgrid-scale gradient model for compressible magnetohydrodynamics turbulent instabilities, Phys. Fluids **31**, 105102 (2019).

[13] F. Carrasco, D. Viganò, and C. Palenzuela, Gradient subgrid-scale model for relativistic MHD Large Eddy simulations, Phys. Rev. D **101**, 063003 (2020).

[14] E. R. Most, Impact of a mean field dynamo on neutron star mergers leading to magnetar remnants, Phys. Rev. D **108**, 123012 (2023).

[15] A. Brandenburg and K. J. Donner, The dependence of the dynamo alpha on vorticity, Mon. Not. R. Astron. Soc. **288**, L29 (1997).

[16] O. Gressel and M. E. Pessah, Characterizing the mean-field dynamo in turbulent accretion disks, Astrophys. J. **810**, 59 (2015).

[17] J. D. Hogg and C. Reynolds, The influence of accretion disk thickness on the large-scale magnetic dynamo, Astrophys. J. **861**, 24 (2018).

[18] A. B. Bendre, K. Subramanian, D. Elstner, and O. Gressel, Turbulent transport coefficients in galactic dynamo simulations using singular value decomposition, Mon. Not. R. Astron. Soc. **491**, 3870 (2020).

[19] P. Dhang, A. Bendre, P. Sharma, and K. Subramanian, Characterizing the dynamo in a radiatively inefficient accretion flow, Mon. Not. R. Astron. Soc. **494**, 4854 (2020).

[20] É. Racine, P. Charbonneau, M. Ghizaru, A. Bouchat, and P. K. Smolarkiewicz, On the mode of dynamo action in a global large-eddy simulation of solar convection, Astrophys. J. **735**, 46 (2011).

[21] K. Kiuchi, A. Reboul-Salze, M. Shibata, and Y. Sekiguchi, A large-scale magnetic field produced by a solar-like dynamo in binary neutron star mergers, Nat. Astron. **8**, 298 (2024).

[22] J. Jacquemin-Ide, F. Rincon, A. Tchekhovskoy, and M. Liska, Magnetorotational dynamo can generate large-scale vertical magnetic fields in 3D GRMHD simulations of accreting black holes, Mon. Not. R. Astron. Soc. **532**, 1522 (2024).

[23] Z. B. Etienne, V. Paschalidis, R. Haas, P. Mösta, and S. L. Shapiro, IllinoisGRMHD: An open-source, user-friendly GRMHD code for dynamical spacetimes, Classical Quantum Gravity **32**, 175009 (2015).

[24] S. C. Noble, C. F. Gammie, J. C. McKinney, and L. Del Zanna, Primitive variable solvers for conservative general relativistic magnetohydrodynamics, Astrophys. J. **641**, 626 (2006).

[25] C. F. Gammie, J. C. McKinney, and G. Toth, HARMHARM: A Numerical scheme for general relativistic magnetohydrodynamics, Astrophys. J. **589**, 444 (2003).

[26] W. P. Jones and B. E. Launder, The prediction of laminarization with a two-equation model of turbulence, Int. J. Heat Mass Transfer **15**, 301 (1972).

[27] S. B. Pope, *Turbulent Flows, 1st Edition* (Cambridge University Press, Cambridge, England, 2000).

[28] S. Kenjereś and K. Hanjalić, On the implementation of effects of Lorentz force in turbulence closure models, Int. J. Heat Fluid Flow **21**, 329 (2000).

[29] Z. Meng, S. Zhang, J. Jia, Z. Chen, and M. Ni, A K-epsilon rans turbulence model for incompressible MHD flow at high Hartmann number in fusion liquid metal blankets, Int. J. Energy Res. **42**, 314 (2018).

[30] D. Radice, General-relativistic Large-Eddy simulations of binary neutron star mergers, Astrophys. J. Lett. **838**, L2 (2017).

[31] M. D. Duez, A. Knight, F. Foucart, M. Haddadi, J. Jesse, F. Hebert, L. E. Kidder, H. P. Pfeiffer, and M. A. Scheel, Comparison of momentum transport models for numerical relativity, Phys. Rev. D **102**, 104050 (2020).

[32] T. W. Baumgarte and S. L. Shapiro, General—relativistic MHD for the numerical construction of dynamical space—times, Astrophys. J. **585**, 921 (2003).

[33] O. Porth *et al.* (Event Horizon Telescope Collaboration), The Event Horizon general relativistic magnetohydrodynamic code comparison project, Astrophys. J. Suppl. Ser. **243**, 26 (2019).

[34] Z. B. Etienne, Y. T. Liu, and S. L. Shapiro, Relativistic magnetohydrodynamics in dynamical spacetimes: A new AMR implementation, Phys. Rev. D **82**, 084031 (2010).

[35] K. A. Sorathia, C. S. Reynolds, J. M. Stone, and K. Beckwith, Global simulations of accretion disks I: Convergence and comparisons with local models, Astrophys. J. **749**, 189 (2012).

[36] R. Narayan, A. SÄ dowski, R. F. Penna, and A. K. Kulkarni, GRMHD simulations of magnetized advection-dominated accretion on a non-spinning black hole: Role of outflows, Mon. Not. R. Astron. Soc. **426**, 3241 (2012).

[37] P. Dhang and P. Sharma, 3D global simulations of RIAFs: Convergence, effects of azimuthal extent and dynamo, Mon. Not. R. Astron. Soc. **482**, 848 (2019).

[38] M. T. P. Liska, A. Tchekhovskoy, and E. Quataert, Large-scale poloidal magnetic field dynamo leads to powerful jets in GRMHD simulations of black hole accretion with toroidal field, Mon. Not. R. Astron. Soc. **494**, 3656 (2020).

[39] K. Hayashi, S. Fujibayashi, K. Kiuchi, K. Kyutoku, Y. Sekiguchi, and M. Shibata, General-relativistic neutrino-radiation magnetohydrodynamic simulation of seconds-long black hole-neutron star mergers, Phys. Rev. D **106**, 023008 (2022).

[40] J. H. Krolik, J. F. Hawley, and S. Hirose, Magnetically driven accretion flows in the Kerr metric. IV. Dynamical properties of the inner disk, Astrophys. J. **622**, 1008 (2005).

[41] S. C. Noble, J. H. Krolik, and J. F. Hawley, Dependence of inner accretion disk stress on parameters: The Schwarzschild case, Astrophys. J. **711**, 959 (2010).

[42] K. Beckwith, J. Hawley, and J. Krolik, Where is the radiation edge in magnetized black hole accretion discs?, Mon. Not. R. Astron. Soc. **390**, 21 (2008).

[43] R. Aguilera-Miret, C. Palenzuela, F. Carrasco, and D. Viganò, Role of turbulence and winding in the development of large-scale, strong magnetic fields in long-lived remnants of binary neutron star mergers, Phys. Rev. D **108**, 103001 (2023).

[44] A. Brandenburg, A. Nordlund, R. F. Stein, and U. Torkelsson, Dynamo-generated turbulence and large-scale magnetic fields in a Keplerian shear flow, Astrophys. J. **446**, 741 (1995).

[45] S. W. Davis, J. M. Stone, and M. E. Pessah, Sustained magnetorotational turbulence in local simulations of stratified disks with zero net magnetic flux, Astrophys. J. **713**, 52 (2010).

[46] T. A. Yousef, A. Brandenburg, and G. Rdiger, Turbulent magnetic prandtl number and magnetic diffusivity quenching from simulations, Astron. Astrophys. **411**, 321 (2003).

[47] X. Guan and C. F. Gammie, The turbulent magnetic Prandtl number of MHD turbulence in disks, Astrophys. J. **697**, 1901 (2009).

[48] S. Fromang and J. M. Stone, Turbulent resistivity driven by the magnetorotational instability, Astron. Astrophys. **507**, 19 (2009).

[49] A. Tchekhovskoy, HARMPI version 1.0, https://github.com/atchekho/harmpi (Released July 19, 2016; Accessed June. 5, 2024).

[50] A. Tchekhovskoy, R. Narayan, and J. C. McKinney, Efficient generation of jets from magnetically arrested accretion on a rapidly spinning black hole, Mon. Not. R. Astron. Soc. **418**, L79 (2011).